Eur. Phys. J. D **32**, 83–93 (2005)
DOI: 10.1140/epjd/e2004-00200-6

THE EUROPEAN PHYSICAL JOURNAL D

Storage ring free electron laser dynamics in presence of an auxiliary harmonic radio frequency cavity

C.A. Thomas[1,2,a], J.I.M. Botman[1], C. Bruni[2], G. Orlandi[2], G. de Ninno[3], D. Garzella[2], and M.E. Couprie[2]

[1] Applied Physics Department, Technische Universiteit Eindhoven, The Netherlands
[2] LURE, Université Paris-Sud, France
[3] Sincrotrone Trieste, Italy

Received 3 August 2004
Published online 4 January 2005 –

Abstract. In a Storage Ring Free Electron Laser (SRFEL) there is a strong interdependence between the laser beam and the electron beam from which the laser is generated. The Super ACO storage ring has a second Radio Frequency (RF) cavity at the 5th harmonic of the main RF cavity. It is used to shorten the bunch length, thereby enhancing the laser gain. Employing this RF harmonic cavity instabilities are observed with a strong effect on both the laser radiation properties and the electron beam behaviour. In this paper, we first present beam characteristics of Super-ACO as influenced by the harmonic cavity, and the instabilities of the beam due to this RF cavity. Then we discuss the FEL properties in presence of the harmonic RF cavity. In general the harmonic cavity functions as intended, and it is observed that the laser suppresses the instabilities caused by the harmonic cavity in the absence of the FEL.

PACS. 41.60.Cr Free-electron lasers – 05.45.-a Nonlinear dynamics and nonlinear dynamical systems – 29.20.Dh Storage rings – 41.75.Fr Electron and positron beams

Highlight Paper

1 Introduction

Free Electron Lasers (FELs) are coherent tunable and powerful sources, covering the wavelength range from IR to VUV. They are based on the interaction of light with a relativistic electron beam that travels through the permanent sinusoidal magnetic field of an undulator [1]. While traversing the undulator the electrons bend and emit synchrotron radiation: the spontaneous emission of the FEL. The interaction, at each passage, of a light pulse with an electron bunch leads to laser gain, with a simultaneous loss of energy of the electrons. In a storage ring free electron laser, the electrons, or positrons, are re-circulated and interact at each passage in the laser optical cavity with the light pulse. The interaction leads to the amplification of the light pulse and induces energy spread in the electron beam. As the gain depends on the energy spread, the enhancement of energy spread of the electron beam is responsible for the storage ring free electron laser saturation [2].

The first FEL operation was demonstrated in the IR on a linear accelerator in 1977 [2]. In 1983 the first lasing on a storage ring was obtained at Anneau de COllision d'Orsay (collision ring ACO), in the visible wavelength range [3]. Nowadays, storage ring free electron lasers (SRFEL) in rings like Super-ACO [4], ELETTRA [5], DELTA [6], DUKE [7], UVSOR [8], NIJI-IV [9] are operating on a regular basis in the UV and VUV range.

These UV-VUV SRFELs provide a unique tool for performing time-resolved and/or frequency resolved experiments [10]. Furthermore, the natural synchronization of the FEL pulse with the synchrotron radiation extends the possibilities of the laser to two-color experiments using the complementary features of UV tunable FELs and the broadband spectral range of synchrotron radiation sources [11]. Nevertheless, stringent requirements on the laser stability are needed in order to perform these experiments properly. The laser dynamics is coupled with the electron beam dynamics, consequently a stable laser requires a stable beam.

An auxiliary RF cavity in the ring, operating at a higher harmonic of the main accelerating cavity, is normally used to lengthen the bunch and reduce or damp longitudinal instabilities [12]. At Super-ACO, as before at VEPP 3 [13] and at UVSOR [14], the harmonic cavity is functioning in the bunch shortening mode during FEL operation, in order to enhance the laser gain, which allows to extract more power for user applications. But when this cavity is used, this may also induce instabilities in the beam due to an enhancement of the strength of the wakefield as a result of the increased bunch charge. Therefore, the dynamics of the laser will be modified and consequently the laser characteristics will be different.

[a] e-mail: cyrille.thomas@diamond.ac.uk

For the design and optimisation of SRFELs, 3-dimensional numerical codes have been developed [15–17]. Also instabilities such as the microwave instability [18] and coherent synchrotron oscillations [19], and the interplay between the beam instability and the FEL, need to be taken into account in order to understand the dynamics of SRFELs and possibly to control it. We developed a 1-dimensional numerical code [20] for investigating the dynamics of the SRFEL in the presence of the microwave instability. The code is based on earlier work of Dattoli [21, 22]. The code has provided qualitative as well as quantitative results in agreement with measurements performed at the Super ACO and ELETTRA FELs [23]. The code showed the competition between the FEL induced beam phenomena and the other beam instabilities. From that competition several situations may arise: first the laser damps all the instabilities and the laser becomes relatively stable; second, the instabilities switch off the FEL and perturb the beam; finally, the FEL may co-exist with the beam instabilities, providing a less stable FEL with longitudinal jitter and intensity fluctuations, as well as a perturbed electron beam. So far, the code was restricted to storage rings operating with the fundamental RF cavity alone.

In this paper, we present the beam dynamics induced by the 5th harmonic RF cavity at Super-ACO: we describe the longitudinal bunch characteristics as a function of the harmonic cavity parameters, the various instabilities observed and their sources. Then we analyse the properties and the dynamics of the FEL. Finally, we discuss the interplay between the laser and the beam.

2 Characterization of the beam

The 5th harmonic cavity used for bunch length shortening induces effects, which are different from the situation in which this cavity is not present. In particular, various instabilities show up, which cannot immediately be explained by theoretical models that are successful for the case in which the harmonic cavity is absent. In this section, we first briefly describe the measurement equipment at Super ACO used for the determination of bunch length and energy spread. Then, we present measurements as a function of beam current and of harmonic cavity voltage. We ascribe observed phenomena and instabilities to effects such as the microwave instability and the potential well distortion. This section only describes the bunch characteristics when the FEL is off. The combined features of the FEL and electron beam in the storage ring are the subject of the subsequent section.

2.1 Measurement apparatus for the study of the longitudinal beam dynamics

The longitudinal beam parameters are measured at Super-ACO respectively with a Double Sweep Streak Camera DSSC (Hamamatsu) for describing the temporal bunch distribution and a CCD camera for the bunch energy distribution. The DSSC is illuminated with the synchrotron radiation from a bending magnet, where the synchrotron light pulse has the temporal profile of the electron bunches. A cut of a DSSC image [24] (Fig. 1), taken at a given beam current, along the fast sweep (vertical) gives the temporal bunch distribution, and the time evolution of the temporal distribution can be followed along the slow time scale (horizontal). The moments of the distribution provide further information: on each image one can extract the values vs. time of the bunch centroid (moment of first order), the r.m.s bunch length (moment of second order), and the skewness and kurtosis (moment of 3rd and 4th order respectively).

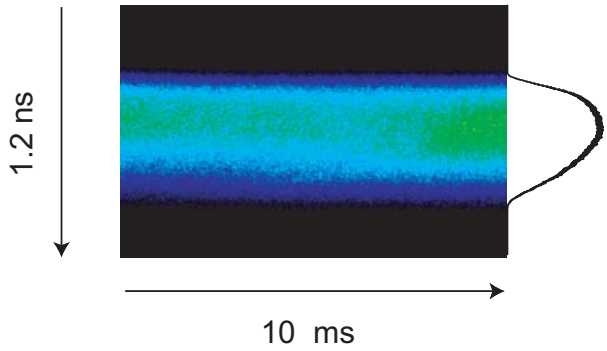

Fig. 1. Image of the bunch temporal distribution obtained with Hamamatsu DSSC at the total current $I = 41$ mA. The moment method, applied on the distribution shown on the right side of the image, give the following values: the bunch length $\sigma_\tau = 140$ (ps).

The energy distribution and its second order moment, the energy spread (σ_ϵ), is obtained from the measurement, on a CCD image, of the horizontal beam dimension in a dispersive section of the ring [25]. The following relation is used:

$$\sigma_x^2 = \epsilon_x \beta_x + (\eta \sigma_\epsilon)^2, \quad (1)$$

where σ_x is the r.m.s horizontal beam size, ϵ_x, β_x and η are respectively the horizontal beam emittance, the beta function and the dispersion function at the measurement point. A Gaussian is always the best fit of the distribution function for extracting the values of the energy spread. The parameters of the Super ACO FEL are given in Table 1.

The DSSC also provides information on the laser pulse similar as for the electron bunch temporal distribution, i.e. the pulse duration, the pulse centroid, etc.

For the measurement of the synchrotron oscillation frequency a spectrum analyser is employed.

2.2 Longitudinal beam properties

The longitudinal phase space distribution of an electron bunch in the storage ring gets its shape from several contributions [26–28]. The natural (i.e. near zero beam current) energy and position distributions have a Gaussian shape, and the bunch length is proportional to the natural energy spread. Collective effects show up when the

Table 1. Super-ACO FEL parameters.

storage ring		**FEL constituting elements**	
E_0 (MeV)	800	Cavity length (m)	18
T_0 (ns)	240		
α_c	0.0148	Optical klystron length (m)	3.1
$\sigma_{\epsilon,0}$	5.4×10^{-4}	undulators period length (cm)	12.9
ν_{RF} (MHz)	100	N	10
ν_{hRF} (MHz)	500	N_d	80–100
V_{RF} (kV)	170		
V_H (kV)	0–280	**FEL characteristics**	
β_x (m)	1.528	r.m.s pulse duration (ps)	10
η(m)	0.364	beam-waist (μm)	400
ϵ_x (m)	2.7×10^{-8}	Maximum average output power (350 nm) (mW)	300

beam current is increased: this is the result of the wake-field generated by the relativistic electrons, reflected by the vacuum chamber and acting back on the generating electron bunch or on the next bunch. The beam gets perturbed and several situations may arise: either there is damping of the perturbation leading as a net effect to the increase of the equilibrium bunch dimensions, or persistent coherent oscillation modes may be generated in the bunches.

In the case of a static bunch, the longitudinal phase space distribution is characterized by a Gaussian energy distribution and by a temporal distribution described by the Haissinski equation [27]. The shape of the energy distribution can be observed on CCD camera images. In general, the solution of the Haissinski equation is not Gaussian. For particular vacuum chamber impedance cases, such as purely resistive or purely inductive impedance, analytical solutions of the Haissinski equation exist [28,29]. However, in general the impedance of a storage ring has both inductive and resistive components [28–31]. The resulting distribution is tilted towards the head of the bunch due to the resistive part of the impedance, and it has a wider shape than Gaussian ('parabolic') due to the inductive part.

Figure 2 shows a comparison between the Gaussian shape and the distributions found solving the Haissinski equation in the case of purely resistive and inductive impedances. Here typical parameters of Super ACO have been used (see caption for details).

Next we turn to measured distributions. Figure 3 gives the measured temporal distribution for Super ACO for several values of the beam current and in the case the harmonic cavity has been switched off. The distributions have been normalized similarly as in Figure 2. From this figure, we conclude that both resistive and inductive components are present as the distribution is both tilted and parabolic. The distortion of the distribution increases with higher beam current. Similarly, the distortion becomes more pronounced when the harmonic cavity voltage is increased. Figure 4 shows the measured temporal distribution for several current values at $V_H = 90$ kV, where V_H is the harmonic cavity voltage. This figure points to the

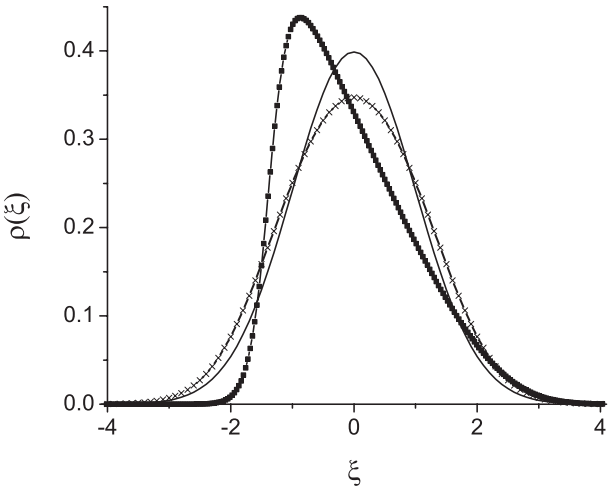

Fig. 2. Bunch temporal distribution, $\rho(\xi)$, from the Haissinski equation, in the pure resistive (square), with $R = 1.5$ kΩ and the current $I = 50$ mA, and inductive cases (cross), at the same current and $L = 20\,\mu$H, compared to the Gaussian distribution (line).

complex nature of the wake as influenced by the harmonic cavity.

In Figure 5 we present the measured values of σ_τ and σ_ϵ (bunch length and energy spread) in Super ACO as a function of the beam current for four values of the harmonic cavity voltage. We discuss this figure in some detail. Note that measurements like this are taken during one shift, with the beam current slowly decreasing from the value at injection to almost zero. Three characteristic current zones can be observed and distinguished for each curve: a high current zone (III), an intermediate zone (II) and a small zone (I) near zero current (up to about 10 mA). The high current zone is characterized by an almost linear increase of both σ_τ and σ_ϵ with beam current. In the intermediate zone, which starts between 40 mA and 30 mA and ends near 10 mA, a strong variation in both quantities occurs and it turns out that rather violent instabilities are exited here. The transition from zone (III) to zone (II) is at a current we call the 'anti-threshold

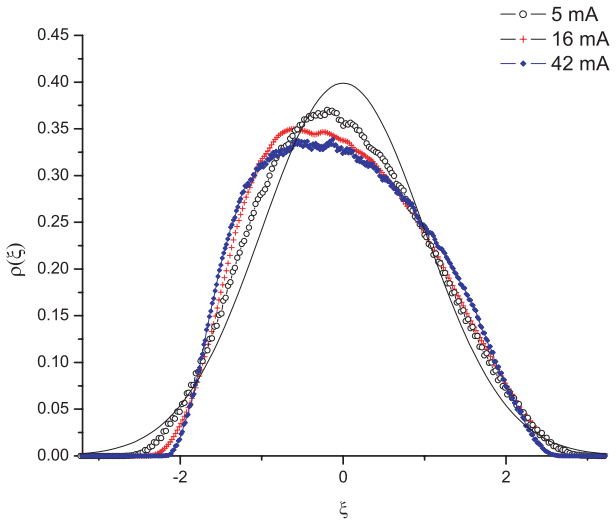

Fig. 3. Bunch temporal distribution of Super ACO, $\rho(\xi)$, measured with the DSSC camera, for several values of the current at $V_H = 0$ kV, and compared to the Gaussian distribution (line). The longitudinal coordinate, ξ, is centered, so that the first order moment of the distribution is at $\xi = 0$, and reduced, so that the second order moment is equal to 1.

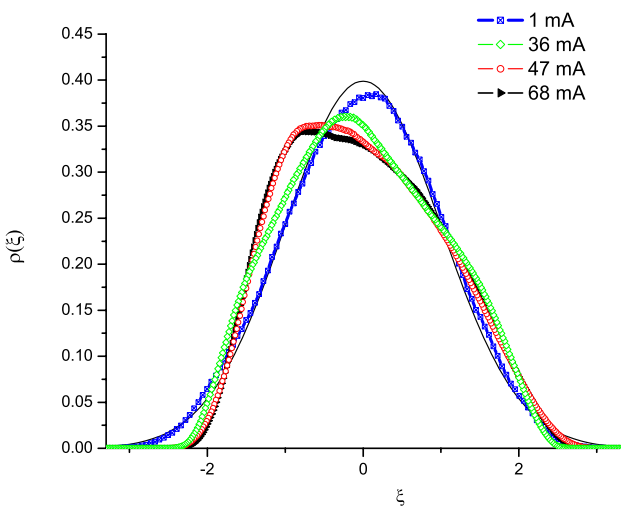

Fig. 4. Bunch temporal distribution measured with the DSSC camera, for several values of the current at $V_H = 90$ kV, and compared with the Gaussian distribution (line).

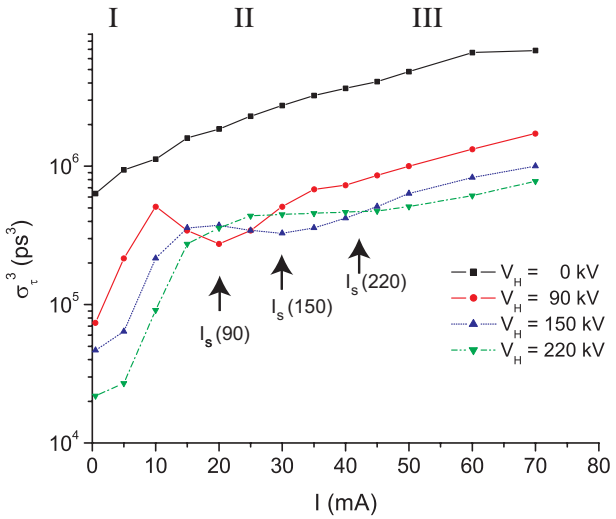

(a) Bunch length

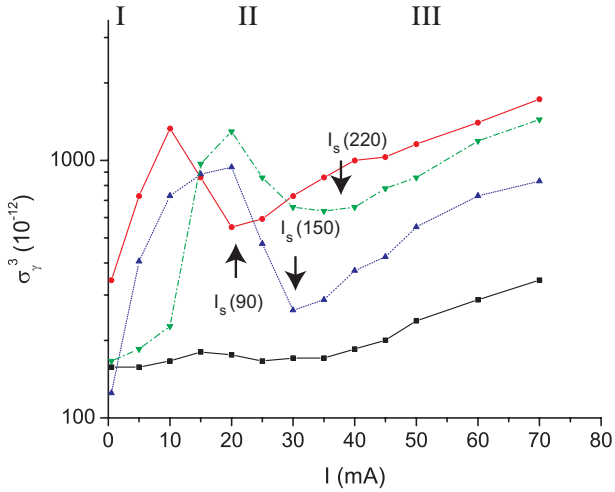

(b) Energy spread

Fig. 5. Bunch length and energy spread vs. current, measured at Super ACO, for several values of V_H.

current' (I_s), as these instabilities are excited for currents lower than I_s. It is given by the local minimum of both σ_τ and σ_ϵ curves.

Figure 6 shows an energy spread of $\sigma_\epsilon = 5.4 \times 10^{-4}$ for all values of V_H in zone (I). This value is consistent with that of the natural energy spread in the low current, single-particle analysis [25]. In this analysis the bunch length, σ_τ is given in terms of the main cavity voltage V_{RF}, voltage V_H, the momentum compaction factor α_c, the harmonic number h and the natural energy spread:

$$\sigma_\tau(0) = \frac{\alpha_c}{\Omega_s(V_H)} \sigma_{\epsilon,0} \tag{2}$$

$$\Omega_s(V_H) = \Omega_{s,0} \sqrt{1 + h \frac{V_H}{V_{RF}}}, \tag{3}$$

with $\Omega_{s,0} = (\alpha_c V_{RF} \omega_{RF} / T_0 E_0)^{1/2}$ the synchrotron angular frequency with the main RF cavity alone, T_0 is the revolution period, E_0 is the electron energy and ω_{RF} the angular RF frequency.

Highlight Paper

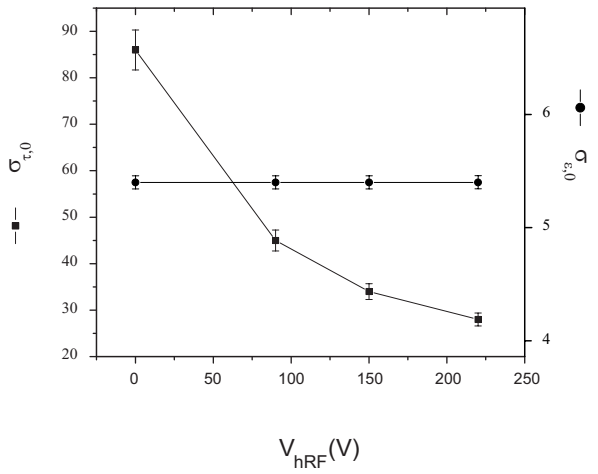

Fig. 6. Relative energy spread (points) and bunch length (squares), measured at Super ACO, at near zero current ($I = 0.5$ mA) for several values of the harmonic cavity voltage.

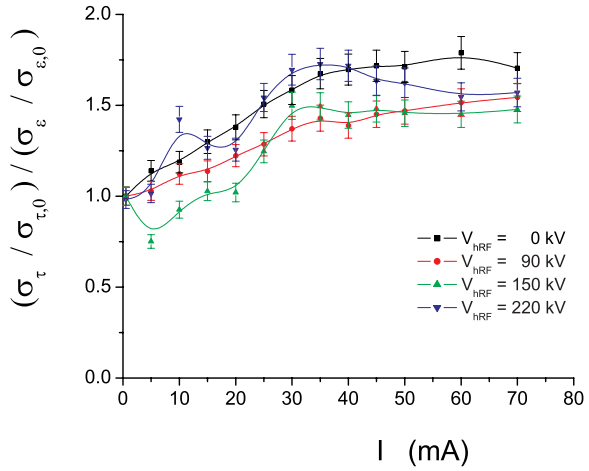

Fig. 7. Ratio of the normalized bunch length with the normalized energy spread vs. average current for the same values of the RF harmonic cavity voltage, V_H, as in Figure 5.

We return to Figure 5. One finds that in zone (III) σ_τ and σ_ϵ are proportional to I^α. This is a characteristic feature of the microwave instability [32–34]. A fit through the measured points gives the value $\alpha \approx 0.8$. The microwave instability is the instability resulting from the interaction of the electrons with that part of the wakefield of which the wavelength lies in the micrometer range. The current threshold where the microwave instability sets on has been given by Boussard [32] and depends on the normalized ring impedance Z_n/n and the synchrotron tune, ν_s, as follow [33]

$$I_{th} = \frac{(\sqrt{2\pi}\,\alpha_c^2 \sigma_{\epsilon,0}^3 (E_0/e))}{\nu_s \frac{Z_n}{n}}, \qquad (4)$$

where e is the elementary charge. Considering an impedance $Z_n/n \approx 4\Omega$ [33] the Boussard threshold, at $V_H = 90$ kV, is $I_{th} \approx 5$ mA. The fact that turbulent bunch lengthening (the microwave instability) is clearly visible only in zone (III) means that in zone (II) other effects dominate, but not that it is absent there.

Finally, we discuss the intermediate zone (II). Experimentally it is evident that specific instabilities occur in this zone, which we define below. The width of zone (II) depends on V_H: $I_s \approx 40$ mA for $V_H = 220$ kV, 30 mA for $V_H = 150$ kV and 20 mA for $V_H = 90$ kV: I_s increases with increasing V_H. No anti-threshold is observed with the passive harmonic cavity. We want to argue that the potential well distortion (PWD) plays an important role in this zone, occurring when the wakefield of the bunch distorts the RF cavity field with a resulting bunch lengthening (see Haissinski [27]). Furthermore, strong coherent oscillations can also be excited in zone (II).

Characteristic of the PWD is the fact that σ_τ increases with beam current I, whereas σ_ϵ remains constant. This feature is clearly observed in Figures 5a and 5b for the passive harmonic cavity ($V_H = 0$ kV) up to about 35 mA, the beginning of zone (III). The ratio $(\sigma_\tau/\sigma_{\tau,0})/(\sigma_\epsilon/\sigma_{\epsilon,0})$, with $\sigma_{\tau,0}$ and $\sigma_{\epsilon,0}$ the values at $I = 0$ mA, increases from 1 near $I = 0$ mA up to 1.7 at $I = 35$ mA. In zone (III) the microwave instability is dominant and σ_τ is proportional to σ_ϵ. As a result the ratio approaches a constant, 1.7. In Figure 7, $(\sigma_\tau/\sigma_{\tau,0})/(\sigma_\epsilon/\sigma_{\epsilon,0})$ is given for all values V_H, as extracted from Figures 5a and 5b. Figure 7 shows similar behavior for all these curves. We conclude that the PWD effect is present in zone (II).

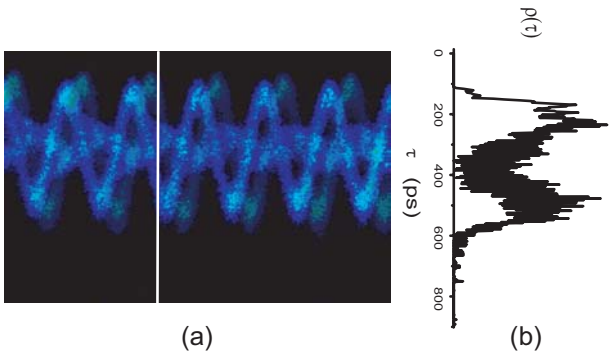

Fig. 8. (a) DSSC image showing the evolution of the perturbed temporal bunch distribution, at a current $I = 32$ mA, just after the instability sets on when the total current is below the 'anti-threshold', $I_s \approx 33$ mA with $V_H = 150$ kV. The bunch distribution is split in three parts oscillating at near the harmonic 2 of the synchrotron frequency $2f_s = 30$ kHz. $V_H = 150$ kV, one bunch mode (horizontal scale: 200 μs, vertical scale: 800 ps). (b) Bunch temporal distribution, $\rho(\tau)$, extracted from the DSSC image (a). $V_H = 150$ kV.

At higher beam currents coherent oscillations are excited in the bunch, as evidenced in spectrum analyzer images and in more detail in streak camera images. Figure 8 shows such a streak camera picture, with a temporal electron distribution taken at the end of zone (II) and displaying separate parts of the bunch oscillating at the second harmonic of the synchrotron frequency, but in phase opposition with respect to each other.

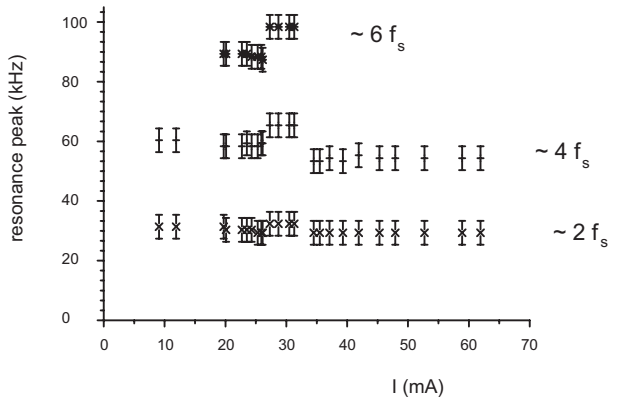

Fig. 9. Resonance peak of the coherent synchrotron oscillations observed with a spectrum analyzer in function of the current, $V_H = 150$ kV. f_s is the synchrotron frequency.

The spectrum analyzer pictures are taken for measuring the synchrotron oscillation frequency. In general they show resonance peaks separated from the central frequency peak, which is at a harmonic of the revolution frequency. Figure 9 presents these resonance peaks as a function of the current and recorded during one shift, for $V_H = 150$ kV.

In general the first and higher order moments of the electron distribution oscillate at frequencies near f_s or at higher harmonics of f_s. It means that coherent oscillations have been excited, for the bunch as a whole or for parts of the bunch (two, three), which oscillate independently. For a dipolar oscillation the first order moment oscillates at $2f_s$, for quadrupolar oscillation the second order moment oscillates at $4f_s$, etc.

Figure 9 shows that coherent oscillations are always present from high to low current. Even sextupolar coherent oscillations appear in zone (II). We note that the amplitude of a side peak with respect to that of the central peak is proportional to the number of electrons performing a particular coherent oscillation. In zone (III) these amplitudes are rather small, in zone (II) these amplitudes are comparable to that of the central peak: substantial parts of the bunch undergo separate coherent oscillations and the resulting instability is quite strong. Figure 8 shows such a typical behavior.

A simple model has been used [24] to reproduce the instability modes observed at Super ACO with the harmonic cavity, from the simple coherent synchrotron oscillation to complex modes like the fish-bones instability [35] (named as such due to its appearance on a DSSC image). The wake field is a function of the electronic density and is modelled by a decaying exponential multiplied by a periodic function, where the decay time constant as well as the period depend on the impedance of the ring [24]. The simple model suggests that the observed collective oscillating modes of the electrons in the bunch derive from a relatively short decay time constant of the wakefield, so that the wake field interacts only with the electrons of the same bunch, the instability being a single bunch instability. In addition, the wakefield responsible for the complex modes observed in zone (II) may explain the appearance of the anti-threshold: the instability starts when the electron density is sufficiently high and the induced wakefield is sufficiently strong to perturb nearest neighbours. In zone (III) the microwave instability takes care that the electron density is low enough. At lower current and higher density the wake field is sufficiently strong to perturb nearest neighbours and excite strong coherent oscillations.

We conclude that complex instabilities and coherent oscillations are present in zone (II), which are different from the situation in which only the main RF cavity is used. An important phenomenon appears to be the potential well distortion, which dominates when the effect of the microwave instability is reduced during the slow decrease of beam current in one shift of the storage ring.

The dynamics of the electron beam and the different perturbations that are present in the beam are important because they influence the SRFEL dynamics. The longitudinal instabilities observed here modify the electron bunch parameters. These effects on the beam induce perturbations in the laser dynamics and in the laser properties such as gain, stability, etc. This will be described in the next section.

3 Laser-beam dynamics

In this section we discuss the effect of the harmonic cavity on the operation of the FEL: we present the laser properties such as gain, line width tuning range, etc., in presence of the 5th harmonic cavity and show the perturbation of the laser by the instabilities identified in the previous section. The Super-ACO FEL is a pulsed laser with a pulse repetition rate corresponding to the time interval between successive passages of electron bunches in the optical cavity, 4.33 MHz. The FEL uses an optical klystron (OK) [36], which is composed of two undulators separated by a dispersive section. This system enhances micro-bunching of the electrons so that the FEL gain is higher than when an undulator of the same overall size as that of the OK is employed. The Super ACO FEL parameters can be found in Table 1. Measurements on various laser and electron beam properties show that the laser operation itself can be regarded as an electron beam perturbation, which competes with the other instabilities discussed above [37]. This is true both for the situation without and with employing a harmonic cavity. The main function of the harmonic cavity is the intended decrease of bunch length and increase of beam intensity. We point at these effects while discussing the experimental data on the laser and end with a simulation using our 1-D code in which the effect of the harmonic cavity is implemented. This clearly shows the competition between the laser and the microwave instability. In a previous paper [20], we have described the numerical code based on analytical theory for calculating the gain, power, and other main properties of the SRFEL system. It is a "1-D"-code: it is restricted to the longitudinal effects of the system. It turns out that this covers many of the important SRFEL phenomena. We have extended this code to take into account the effect of the harmonic cavity.

This mainly means that the bunch length and the longitudinal bunch distribution are modified. In the code the most important instability affecting the electron beam, the microwave instability, is incorporated through its effect on the energy spread of the electron beam. At several occasions below in the description of measurements on the SRFEL using the harmonic cavity, we have applied the modified code for comparisons.

3.1 Super-ACO FEL gain

An important parameter of FEL dynamics is the gain, defined as the relative increase in laser power for one pass of the electron beam through the undulator system. The gain is a dynamical quantity. One finds the maximum gain when the laser starts; this is called the small signal gain, G_0. The gain changes in time depending on the electron bunch quality degradation.

An analytical expression, which takes into account the optical klystron characteristics and the properties of the electron bunches, gives a good estimation of the gain [36]:

$$G_0 = 2.22 \times 10^{-13} K^2 L_{und}^2 (JJ)^2 \, (N + N_d) \, f \frac{\rho_e F_f}{\gamma^3}, \quad (5)$$

where K is the undulator strength, L_{und} is the length of one undulator, JJ is the difference between the Bessel functions of the first kind of order 0 and 1 with argument $x = K^2/(4 + 2K^2)$, F_f is the filling factor for the transverse overlap of the electrons with the photon beam, N is the number of undulator periods, N_d is the number accounting for the advance of the light with respect to the electrons in the dispersive section expressed in number of laser light wavelengths [36]; $f = f_0 \exp(-8(\pi(N + N_d)\sigma_\epsilon)^2)$ is the modulation rate of the optical klystron spectrum [36] where f_0 is a constant between 0 and 1, σ_ϵ is the relative beam energy spread, ρ_e is the electron density and γ is the Lorentz factor corresponding to the electron energy. In this equation measured values of bunch length and beam width determine the electron density and the measured relative energy spread appears in modulation rate. This expression is used to calculate the small signal gain for several values of the harmonic cavity voltage with FEL off. The results are given in Figure 10. At low currents the maximum gain curves are linear in I and the small signal gain increases with V_H: the harmonic cavity, reducing the bunch length, performs as intended. However, with 1% cavity loss the gain is not sufficient to get the laser started; the threshold current at which this occurs starts is respectively 16, 15, 12 and 5 mA at V_H is 0, 90, 150 and 220 kV, as can be deduced from this figure. Once more these data show the effectiveness of the harmonic cavity. However, equation (5) is entirely a theoretical formula not taking into account any beam instability. Therefore it has to be applied with caution: for those situations in which stable beam phenomena predominate. In the intermediate current zone this is not the case, and G_0 is lower due to extra bunch lengthening and energy spread. The reduction of G_0 is most apparent for the highest values of V_H. Nonetheless, the gain increases by increasing the harmonic cavity voltage, whenever beam instabilities are absent.

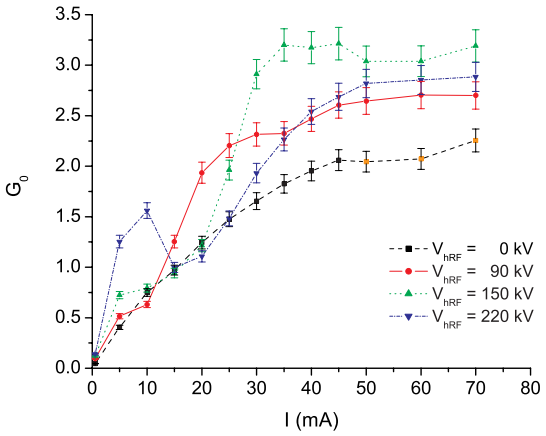

Fig. 10. Maximum gain curves vs. current at 350 nm and for different values of the harmonic cavity voltage V_H, using the expression (5) with an optimized N_d value, $(N + N_d)f = (N + N_d)e^{-8\pi^2(N+N_d)^2(\sigma_\gamma/\gamma)^2} \approx \exp(-1/2)/(4\pi\sigma_\gamma/\gamma)$, and $K = 3.5$, $L_{und} = 1.3$ m, $F_f = 0.9$, $\sigma_x = 380$ (μm), $\sigma_y = 380$ (μm).

3.2 Temporal and dynamical features: the detuning curve

In general the temporal behaviour of the laser is complicated and depends among others on the precise tuning of electron bunches and laser pulses. At Super ACO extensive so-called detuning studies have been undertaken for obtaining insight in the dynamics of the combined electron beam — laser system [23,38,39]. Longitudinal detuning leads to a cumulative delay between laser pulses and electron bunches. A detuning curve presents a particular laser property as function of the detuning, such as laser intensity or pulse duration. We mention that the phenomena regarding detuned lasers are well understood and accurately simulated [23]: allowable tuning range, CW operation, pulsed or intensity modulated behaviour, laser pulse width and bandwidth, etc. Figures 11 and 12 show the laser intensity detuning curve for the passive harmonic cavity case ($V_H = 0$) and for a harmonic cavity voltage of $V_H = 90$ kV. It is seen that under the action of the harmonic cavity the detuning curve becomes asymmetric. The width of the central CW operation zone, a few Hertz, which is the preferred zone for regular operation of the FEL, is reduced, as well as the total width of the detuning curve. Outside the CW region, the laser is modulated for negative detuning and either fully pulsed or modulated for positive detuning, the pulse or modulation frequency being linearly dependent on the detuning value. The symmetry of the detuning curve depends on the symmetry of the temporal bunch distribution, which is influenced by the harmonic cavity. For higher harmonic cavity voltages

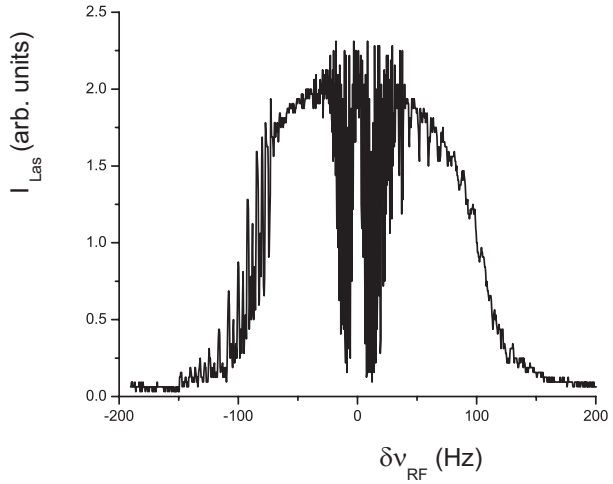

Fig. 11. Detuning curve for the passive harmonic cavity ($V_H = 0$). The current is 39.4 mA.

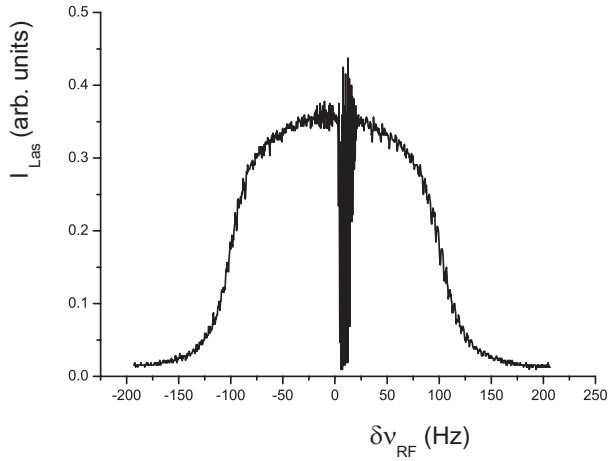

Fig. 12. Detuning curve for $V_H = 90$ kV. The current is 26 mA.

more pulsed or modulated regions for positive detuning are observed. Both by experiments and through simulations it is seen that the detuning curve characteristics such as the total width, depend the laser gain, the cavity loss, the instability strength, etc. These in turn depend on the value of the harmonic cavity voltage.

3.3 Spectral features

Measurements of the laser pulse duration and its spectral width as function of the detuning have shown that the laser operates near the Fourier limit in the narrow central detuning zone [40]. With the harmonic cavity this limit is observed to be closer to the Fourier limit: a factor 2 with harmonic cavity against a factor 10 in the passive case. In addition the pulse duration has been observed to be close to the theoretical limit, given by $\sigma_{las} = \sqrt{\Delta\,\sigma_\tau}$ [41] (where $\Delta = (N + N_d)\lambda_{las}/c$ is the slippage length expressed in s). To operate the SRFEL at the Fourier limit, one of the main requirements is to have stable electron bunches and perfect tuning in the central zone of the intensity detuning graph. It is essential to employ a feedback system [42], which maintains the laser at zero detuning. Under these conditions, the laser pulse is described by the fundamental Super Mode having the shortest pulse duration and the shortest spectral width at the Fourier limit [43].

The spectral tunability of an FEL depends on the undulator strength parameter, $K = 0.94[\mathrm{T}^{-1}\mathrm{cm}^{-1}]\,\lambda_u\,B_u$ (with λ_u the period of the undulator and B_u the amplitude of the periodic magnetic field of the undulator) and furthermore on the reflectivity of the mirrors. At Super ACO, the sets of mirrors allow a global tunability range of [300, 600] nm.

As indicated above, the spectral width of the UV-VUV SRFEL (down to 189 nm for ELETTRA and 300 nm for Super ACO) is a very interesting property. Combined with the short pulse duration, the laser is an ideal tool for performing time resolved spectroscopy [10]. The relative spectral bandwidth, $\Delta\lambda/\lambda$, obtained with an SRFEL is roughly given by the expression [40]:

$$\frac{\Delta\lambda}{\lambda} \approx \frac{1}{\pi}\sqrt{\frac{\lambda}{(N+N_d)c\sigma_\tau}}, \tag{6}$$

with c the speed of light in vacuum. The combination of spectral resolution and time resolution is bounded by the Fourier limit. Typical values are a temporal resolution of 20 ps and a frequency resolution of 2×10^{-4}.

3.4 FEL power

Laser power measurements have been performed at a harmonic cavity voltage of $V_H = 120$ kV as a function of the beam current. The following observations are reported. For lower currents in the high current zone and into the intermediate current zone, the power rises monotonically with beam current, see Figure 13. For the highest currents in the high current zone, measurements are more difficult, with large variations in power values (between 20 and 70 mW), as the equilibrium of the experimental condition are difficult to obtain, and as the MI may play a role and perturb the laser. Theoretically, for an optical klystron the average power that can be extracted is [44]:

$$P_{laser} = \eta_c 8\pi^2 (N+N_d) f \left(\left(\frac{\sigma_\gamma}{\gamma}\right)^2_{on} - \left(\frac{\sigma_\gamma}{\gamma}\right)^2_{off} \right) P_s, \tag{7}$$

where η_c is the ratio between the transmission of the mirrors and the total losses of the cavity, $((\sigma_\gamma/\gamma)^2_{on} - (\sigma_\gamma/\gamma)^2_{off})$ measures the laser induced energy spread of the beam, and $P_s = (2cr_e m_e c^2 T_0/3e)\gamma^4 I/\rho_0^2$ is the synchrotron power, with r_e the electron classical radius, m_e the electron mass, e the electron charge, I the current and ρ_0 the average radius of curvature of the storage ring bending magnets. In Figure 13 we present the power extracted at Super ACO for $V_{hRF} = 120$ kV by simulation, which shows similar behaviour as the measurement. The behaviour of the power vs. current is found to be proportional to $I^{\beta'}$ (where $\beta' \approx 0.8$, see Fig. 13).

Highlight Paper

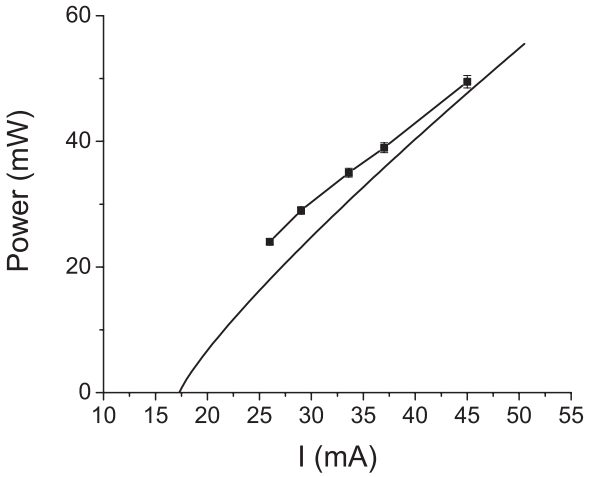

Fig. 13. Laser power vs. current (points) for $V_H = 120$ kV, compared with simulation results for the same experimental condition (solid line). The fit of the two curves has been done with the formula: $P = b(I - I_{th})^{\beta}$. The fit provides the same threshold current for the lasing condition, $I_{th} = 17$ mA, and the exponent $\beta \approx 0.8$.

The measured power as the current decreases does not show any transition between the high current regime, with clear evidence of the microwave instability, and the intermediate current regime with different and stronger instabilities. This shows that the laser is in competition with these instabilities, in particular with the microwave instability. When the laser starts, it damps the instabilities, therefore no transition should be observed.

3.5 Competition between the FEL and the beam instabilities

As seen in the previous section the FEL gain and the extracted power may be reduced by perturbations of the electron beam. A first effect of the laser, observed at VEPP3 [13] and UVSOR [45], is "heating" of the beam. The FEL induces extra beam energy spread, with proportional bunch lengthening.

At Super-ACO, the FEL induced heating of the beam has also been observed: a difference in energy spread for laser on and off has been measured in excess of 10%. In addition to only heating the beam, the laser damps beam instabilities. As observed on the spectrum analyzer, the quadrupolar coherent synchrotron oscillations disappear with laser on, and reappear with laser off.

As has been described in [37] the laser induced energy spread shifts the Boussard threshold current and prevents the start-up of the microwave instability.

These results have been reproduced with simulations using the before mentioned 1-D code. We made simulations for the case of Super ACO, $V_H = 90$ kV for perfect longitudinal tuning for two values of the beam current: $I = 100$ mA (a), and $I = 60$ mA (b). Figure 14 shows the result of these simulations: the intra cavity dimensionless

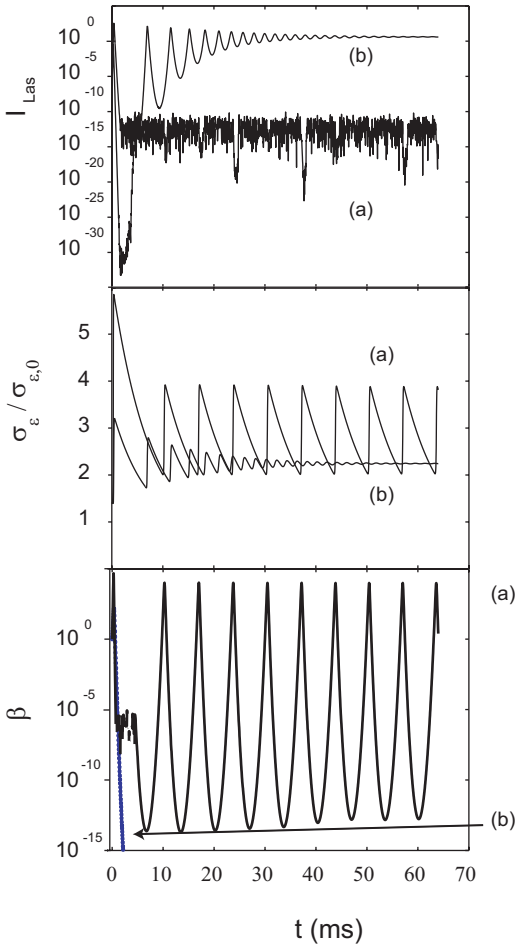

Fig. 14. Simulation for the case of Super ACO with $V_H = 90$ kV and the current $I = 100$ mA (a) and $I = 60$ mA (b). **Top**: Laser dimensionless intra-cavity power, I_{las}. The power density is given by $P = I_{las} I_{sat}$ [20] with $I_{sat} = 690(\gamma/N)^4/(K\,\lambda_u f_b(\xi))^2$ MW cm^{-2}, where $\gamma = 1566.55$ is the Lorentz factor of the electrons, $N = 44$ is the number of undulator period (for the equivalent undulator to the Super ACO optical klystron), $K = 3.3$ is the undulator strength, $\lambda_u = 0.13$ m, and $f_b(\xi)$ is the difference between the first kind Bessel functions of zero and first order with the argument $\xi = K^2/(4 + 2K^2)$. **Middle**: relative energy spread, $\sigma_\epsilon/\sigma_{\epsilon,0}$. **Bottom**: microwave instability growth rate, β.

power, relative energy spread and the microwave instability growth rate versus time.

For case (a) the small signal gain is $g_0 = 3\%$ and the microwave instability strength has been calculated using a normalized impedance $Z_n/n = 4\Omega$, as found in [33]. The laser starts, but the microwave instability is too strong and switches off the laser, as can be seen in Figure 14. Then the induced relative energy spread oscillates as in the characteristic sawtooth regime of the microwave instability.

In case (b), the small signal gain is $g_0 = 2.5\%$, the gain is smaller but the microwave instability strength is also smaller. The laser starts, reaches saturation, and the laser induced relative energy spread is high enough to switch the

microwave instability off and to prevent it from starting again, as shown by Figure 14. The laser characteristics in that simulation are close to the non-perturbed case. But for example the pulse duration $\sigma_{las} = 20$ ps, in agreement with the measurements, is longer than in the ideal case without instability (numerical), $\sigma_{las} = 7$ ps. The latter value is close to the theoretical value given by the Super Mode model [41], $\sigma_{las,th} = 3$ ps. The laser reaches the saturation and the energy spread is stable and set as well to a level which depends on the laser intensity saturation.

Whenever the laser starts, the electron beam longitudinal instabilities are damped and the electron beam is stabilised. At very high current values, the strength of the MI, which depends on the bunch length and consequently on V_H and on the impedance of the ring, may be strong enough to prevent the laser from starting.

We observe experimentally the laser is not always stable at very high current. In addition, as shown in Figure 13, once the laser sets on, the beam become more stable, and the laser power decreases with the current, showing neither transition nor instabilities.

In summary, in the range of current where the laser can start, the laser can be seen as a beam stabiliser as it is able to damp the beam instabilities, and as a consequence the laser self-stabilizes. This holds in particular for the instabilities in the intermediate current regime.

4 Conclusion

Beam properties have been studied for an electron storage ring employing a higher harmonic cavity in addition to the main RF cavity, in particular for the consequences for operating a Free Electron Laser. These studies have been performed for the case of Super ACO. Without the FEL, instabilities are observed for beam currents below a certain critical value ("anti-threshold"). Above this value the microwave instability is dominant in most cases; below the anti-threshold, stable beam is dominated by the potential well distortion. When the FEL is switched on, the FEL competes with the instabilities mentioned above. By the FEL operation these instabilities may be suppressed. Simulations employing a one-dimensional analysis of electron beam behaviour and laser dynamics show this competition. The intended effect of the harmonic cavity: shortening electron bunches and thereby increasing the laser gain, works. The best operating condition for the FEL is for beam currents in the range 20 to 60 mA at a harmonic cavity voltage of 150 kV. Then the laser works very near to the Fourier limit, with a pulse width of 20 ps and an energy spread of 4×10^{-4}.

However also bunch lengthening induced by the PWD, bunch lengthening proportional to the increased energy spread induced by the MI and by coherent synchrotron oscillations are found to be the cause of lowering the gain enhancement from the harmonic cavity. The broadband impedance value is the main scaling factor of these phenomena. A large value would severely limit the performance of the FEL.

References

1. J.M.J. Madey, J. Appl. Phys. **42**, 1906 (1971)
2. D.A.G. Deacon, L.R. Elias, J.M.J. Madey, G.J. Ramian, H.A. Schwettman, T.I. Smith, Phys. Rev. Lett. **38**, 892 (1977)
3. M. Billardon, J.M. Ortega, P. Elleaume, C. Bazin, M. Bergher, M. Velghe, Y. Petroff, D.A.G. Deacon, K.E. Robinson, J.M.J. Madey, Phys. Rev. Lett. **51**, 1652 (1983)
4. D. Nutarelli, D. Garzella, E. Renault, L. Nahon, M.E. Couprie, Nucl. Instrum. Meth. Phys. Res. A **445**, 143 (2000)
5. R.P. Walker, J.A. Clarke, M.E. Couprie, G. Dattoli, M. Eriksson, D. Garzella, L. Giannessi, M. Marsi, M.W. Poole, E. Renault, R. Roux, M. Trovò, S. Werin, K. Wille, Nucl. Instrum. Meth. Phys. Res. A **467**, 34 (2001)
6. D. Nölle, D. Garzella, A. Geisler, L. Gianessi, M. Hirsch, H. Quick, M. Ridder, T. Schmidt, K. Wille, Nucl. Instrum. Meth. Phys. Res. A **445**, 128 (2000)
7. V.N. Litvinenko, S.H. Park, I.V. Pinayev, Y. Wu, Nucl. Instrum. Meth. Phys. Res. A **475**, 195 (2001)
8. M. Hosaka, S. Koda, M. Katoh, J. Yamazaki, K. Hayashi, K. Takashima, T. Gejo, H. Hama, Nucl. Instrum. Meth. Phys. Res. A **483**, 146 (2002)
9. K. Yamada, N. Sei, H. Ohgaki, T. Mikado, S. Sugiyama, T. Yamazaki, Nucl. Instrum. Meth. Phys. Res. A **445**, 173 (2000)
10. M.E. Couprie, F. Mérola, P. Tauc, D. Garzella, A. Delboulbé, T. Hara, M. Billardon, Rev. Sci. Instrum. **65**, 1485 (1994)
11. M. Marsi, M.E. Couprie, L. Nahon, D. Garzella, R. Bakker, A. Delboulbé, D. Nutarelli, R. Roux, B. Visentin, C. Grupp, G. Indlekofer, G. Panaccione, A. Taleb-Ibrahimi, M. Billardon, Nucl. Instrum. Meth. Phys. Res. A **393**, 548 (1997)
12. M. Katoh, K. Hayashi, T. Honda, Y. Hori, M. Hosaka, T. Kinoshita, S. Kouda, Y. Takashima, J. Yamazaki, Nucl. Instrum. Meth. Phys. Res. A **467**, 68 (2001)
13. N.A. Vinokurov, I.B. Drobyazko, G.N. Kulipanov, V.N. Litvinenko, I.V. Pinayev, Rev. Sci. Instrum. **60**, 1435 (1989)
14. M. Kamada, H. Hama, Rev. Sci. Instrum. **66**, 2362 (1995)
15. G. Dattoli, A. Dipace, E. Sabia, A. Torre, G.K. Voykov, M. Carpanese, J. Appl. Phys. **80**, 6589 (1996)
16. V.N. Litvinenko, B. Burnham, J.M.J. Madey, Y. Wu, Nucl. Instrum. Meth. Phys. Res. A **358**, 334 (1995)
17. V.N. Litvinenko, Y. Wu, B. Burnham, J.M.J. Madey, Nucl. Instrum. Meth. Phys. Res. A **358**, 349 (1995)
18. G. Dattoli, L. Mezi, M. Migliorati, L. Palumbo, Nuovo Cim. A **112**, 491 (1999)
19. R. Roux, M. Billardon, Nuovo Cim. A **112**, 513 (1999)
20. C.A. Thomas, J.I.M. Botman, G.D. Ninno, M.E. Couprie, L. Mezi, G. Dattoli, Nucl. Instrum. Meth. Phys. Res. A **483**, 181 (2002)
21. G. Dattoli, T. Letardi, A. Renieri, J.M.J. Madey, IEEE J. Quant. Electron. **20**, 1003 (1984)
22. G. Dattoli, Nuovo Cim. A **112**, 507 (1999)
23. C.A. Thomas, J.I.M. Botman, C. Bruni, D. Garzella, M.E. Couprie, G.D. Ninno, G. Dattoli, Nucl. Instrum. Meth. Phys. Res. A (to be published, 2003)
24. R. Roux, M.E. Couprie, T. Hara, R.J. Bakker, B. Visentin, M. Billardon, J. Roux, Nucl. Instrum. Meth. Phys. Res. A **393**, 33 (1997)

25. D. Nutarelli, Ph.D. thesis, Université Paris-Sud, Orsay, France (January 2000)
26. M. Sands, *The physics of electron storage ring, an introduction*, Vol. 121, SLAC report, November 1970
27. J. Haissinski, Nuovo Cim. B **18**, 72 (1973)
28. K. Bane, *Bunch lengthening in the SLC damping ring*, SLAC-PUB Report 5177, SLAC, 1990
29. C.A. Thomas, J.I.M. Botman, R. Bartolini, G. Dattoli, L. Mezi, M. Migliorati, Europhys. Lett. **60**, 66 (2002)
30. A. Hofmann, "Beam instabilities", *CAS: 5th Advanced Accelerator Physics Course*, Chap. 14, Vol. 95-06, CERN Accelerator School, 1995
31. H. Hama, M. Hosaka, Nucl. Instrum. Meth. Phys. Res. A **429**, 172 (1999)
32. D. Boussard, internal report 75-2, CERN, 1975
33. G. Dattoli, L. Mezi, M. Migliorati, A. Renieri, M.E. Couprie, D. Garzella, D. Nutarelli, C. Thomas, G. de Ninno, R. Walker, Nucl. Instrum. Meth. Phys. Res. A **471**, 403 (2001)
34. M. Migliorati, L. Palumbo, G. Dattoli, L. Mezi, Nucl. Instrum. Meth. Phys. Res. A **437**, 134 (1999)
35. R. Roux, Ph.D. thesis, Université Paris-Sud, Orsay, France (January 1999)
36. P. Elleaume, J. Phys. (Paris) **44**, C1-353 (1983)
37. R. Bartolini, G. Dattoli, L. Mezi, A. Renieri, M. Migliorati, M.E. Couprie, G. de Ninno, R. Roux, Phys. Rev. Lett. **87**, 134801 (2001)
38. G. de Ninno, D. Fanelli, M.E. Couprie, Nucl. Instrum. Meth. Phys. Res. A **483**, 177 (2002)
39. G. de Ninno, C. Bruni, D. Nutarelli, D. Garzella, C. Thomas, M.E. Couprie, Phys. Rev. E **67**, 26501 (2003)
40. M.E. Couprie, G. de Ninno, G. Moneron, D. Nutarelli, M. Hirsch, D. Garzella, E. Renault, R. Roux, C. Thomas, Nucl. Instrum. Meth. Phys. Res. A **475**, 229 (2001)
41. G. Dattoli, A. Renieri, Nuovo Cim. B **59**, 1 (1980)
42. M.E. Couprie, D. Garzella, T. Hara, J.H. Codarbox, M. Billardon, Nucl. Instrum. Meth. Phys. Res. A **358**, 374 (1995)
43. G. Dattoli, T. Hermsen, A. Renieri, A. Torre, J.C. Gallardo, Phys. Rev. A **37**, 4326 (1988)
44. D.A.G. Deacon, K.E. Robinson, J.M.J. Madey, C. Bazin, Y. Petroff, M.F. Velghe, M. Billardon, Y. Farge, J.M. Ortega, P. Elleaume, Opt. Commun. **40**, 373 (1982)
45. M. Hosaka, S. Koda, M. Katoh, J. Yamazaki, H. Hama, Nucl. Instrum. Meth. Phys. Res. A **475**, 217 (2001)